Dusty Starbursts Masquerading as Ultra-high Redshift Galaxies in JWST CEERS Observations

Jorge A. Zavala, Véronique Buat, Caitlin M. Casey, Steven L. Finkelstein, Denis Burgarella, Micaela B. Bagley, Laure Ciesla, Emanuele Daddi, Mark Dickinson, Henry C. Ferguson, et al.

The Astrophysical Journal Letters, 943:L9 (14pp), 2023 February 1 https://doi.org/10.3847/2041-8213/acacfe

Dusty Starbursts Masquerading as Ultra-high Redshift Galaxies in JWST CEERS Observations

Jorge A. Zavala[1], Véronique Buat[2], Caitlin M. Casey[3], Steven L. Finkelstein[3], Denis Burgarella[2], Micaela B. Bagley[3], Laure Ciesla[2], Emanuele Daddi[4], Mark Dickinson[5], Henry C. Ferguson[6], Maximilien Franco[3], E. F. Jiménez-Andrade[7], Jeyhan S. Kartaltepe[8], Anton M. Koekemoer[6], Aurélien Le Bail[4], E. J. Murphy[9], Casey Papovich[10,11], Sandro Tacchella[12,13], Stephen M. Wilkins[14,15], Itziar Aretxaga[16], Peter Behroozi[17,18], Jaclyn B. Champagne[3],
and
Adriano Fontana[19], Mauro Giavalisco[20], Andrea Grazian[21], Norman A. Grogin[6], Lisa J. Kewley[22], Dale D. Kocevski[23], Allison Kirkpatrick[24], Jennifer M. Lotz[25], Laura Pentericci[19], Pablo G. Pérez-González[26], Nor Pirzkal[27], Swara Ravindranath[6], Rachel S. Somerville[28], Jonathan R. Trump[29], Guang Yang[30,31], L. Y. Aaron Yung[32], Omar Almaini[33], Ricardo O. Amorín[34,35], Marianna Annunziatella[26], Pablo Arrabal Haro[5], Bren E. Backhaus[29], Guillermo Barro[36], Eric F. Bell[37], Rachana Bhatawdekar[38], Laura Bisigello[21,39], Fernando Buitrago[40,41], Antonello Calabrò[42], Marco Castellano[19], Óscar A. Chávez Ortiz[3], Katherine Chworowsky[3], Nikko J. Cleri[10,11], Seth H. Cohen[43], Justin W. Cole[10,11], Kevin C. Cooke[44], M. C. Cooper[45], Asantha R. Cooray[45], Luca Costantin[26], Isabella G. Cox[8], Darren Croton[46,47], Romeel Davé[48,49], Alexander de la Vega[50], Avishai Dekel[51], David Elbaz[4], Vicente Estrada-Carpenter[52], Vital Fernández[34], Keely D. Finkelstein[3], Jonathan Freundlich[53], Seiji Fujimoto[54,55], Ángela García-Argumánez[56,57], Jonathan P. Gardner[32], Eric Gawiser[58], Carlos Gómez-Guijarro[59], Yuchen Guo[3], Timothy S. Hamilton[60], Nimish P. Hathi[6], Benne W. Holwerda[61], Michaela Hirschmann[62], Marc Huertas-Company[63,64,65], Taylor A. Hutchison[10,11], Kartheik G. Iyer[66], Anne E. Jaskot[67], Saurabh W. Jha[58], Shardha Jogee[3], Stéphanie Juneau[68], Intae Jung[32,69,70], Susan A. Kassin[6,50], Peter Kurczynski[71], Rebecca L. Larson[3], Gene C. K. Leung[3], Arianna S. Long[3], Ray A. Lucas[6], Benjamin Magnelli[4], Kameswara Bharadwaj Mantha[72], Jasleen Matharu[10,11], Elizabeth J. McGrath[23], Daniel H. McIntosh[73], Aubrey Medrano[3], Emiliano Merlin[19], Bahram Mobasher[74], Alexa M. Morales[3], Jeffrey A. Newman[75], David C. Nicholls[76], Viraj Pandya[77], Marc Rafelski[6,50], Kaila Ronayne[10,11], Caitlin Rose[8], Russell E. Ryan, Jr.[6], Paola Santini[19], Lise-Marie Seillé[2], Ekta A. Shah[78], Lu Shen[79,80], Raymond C. Simons[6], Gregory F. Snyder[6], Elizabeth R. Stanway[81], Amber N. Straughn[32], Harry I. Teplitz[82], Brittany N. Vanderhoof[8], Jesús Vega-Ferrero[63], Weichen Wang[50], Benjamin J. Weiner[83], Christopher N. A. Willmer[84], and Stijn Wuyts[85]
(The CEERS Team)
[1] National Astronomical Observatory of Japan, 2-21-1 Osawa, Mitaka, Tokyo 181-8588, Japan
[2] Aix Marseille Univ, CNRS, CNES, LAM Marseille, France
[3] Department of Astronomy, The University of Texas at Austin, Austin, TX, USA
[4] Université Paris-Saclay, Université Paris Cité, CEA, CNRS, AIM, F-91191 Gif-sur-Yvette, France
[5] NSF's National Optical-Infrared Astronomy Research Laboratory, 950 N. Cherry Avenue, Tucson, AZ 85719, USA
[6] Space Telescope Science Institute, 3700 San Martin Drive, Baltimore, MD, USA
[7] Instituto de Radioastronomía y Astrofísica, UNAM Campus Morelia, Apartado postal 3-72, 58090 Morelia, Michoacán, México
[8] Laboratory for Multiwavelength Astrophysics, School of Physics and Astronomy, Rochester Institute of Technology, 84 Lomb Memorial Drive, Rochester, NY 14623, USA
[9] National Radio Astronomy Observatory, 520 Edgemont Road, Charlottesville, VA 22903, USA
[10] Department of Physics and Astronomy, Texas A&M University, College Station, TX 77843-4242, USA
[11] George P. and Cynthia Woods Mitchell Institute for Fundamental Physics and Astronomy, Texas A&M University, College Station, TX 77843-4242, USA
[12] Kavli Institute for Cosmology, University of Cambridge, Madingley Road, Cambridge CB3 0HA, UK
[13] Cavendish Laboratory, University of Cambridge, 19 JJ Thomson Avenue, Cambridge CB3 0HE, UK
[14] Astronomy Centre, University of Sussex, Falmer, Brighton BN1 9QH, UK
[15] Institute of Space Sciences and Astronomy, University of Malta, Msida, MSD 2080, Malta
[16] Instituto Nacional de Astrofísica, Óptica y Electrónica, Luis Enrique Erro 1, Tonantzintla CP 72840, Puebla, México
[17] Department of Astronomy and Steward Observatory, University of Arizona, Tucson, AZ 85721, USA
[18] Division of Science, National Astronomical Observatory of Japan, 2-21-1 Osawa, Mitaka, Tokyo 181-8588, Japan
[19] INAF—Osservatorio Astronomico di Roma, via di Frascati 33, I-00078 Monte Porzio Catone, Italy
[20] University of Massachusetts Amherst, 710 North Pleasant Street, Amherst, MA 01003-9305, USA
[21] INAF—Osservatorio Astronomico di Padova, Vicolo dell'Osservatorio 5, I-35122 Padova, Italy
[22] Harvard-Smithsonian Center for Astrophysics, 60 Garden Street, Cambridge, MA 02138, USA
[23] Department of Physics and Astronomy, Colby College, Waterville, ME 04901, USA
[24] Department of Physics and Astronomy, University of Kansas, Lawrence, KS 66045, USA
[25] Gemini Observatory/NSF's National Optical-Infrared Astronomy Research Laboratory, 950 N. Cherry Avenue, Tucson, AZ 85719, USA
[26] Centro de Astrobiología (CAB/CSIC-INTA), Ctra. de Ajalvir km 4, Torrejón de Ardoz, E-28850 Madrid, Spain
[27] ESA/AURA Space Telescope Science Institute, USA
[28] Center for Computational Astrophysics, Flatiron Institute, 162 5th Avenue, New York, NY 10010, USA
[29] Department of Physics, University of Connecticut, 196 Auditorium Road, Unit 3046, Storrs, CT 06269, USA
[30] Kapteyn Astronomical Institute, University of Groningen, P.O. Box 800, 9700 AV Groningen, The Netherlands
[31] SRON Netherlands Institute for Space Research, Postbus 800, 9700 AV Groningen, The Netherlands
[32] Astrophysics Science Division, NASA Goddard Space Flight Center, 8800 Greenbelt Road, Greenbelt, MD 20771, USA
[33] School of Physics and Astronomy, University of Nottingham, University Park, Nottingham NG7 2RD, UK

[34] Instituto de Investigación Multidisciplinar en Ciencia y Tecnología, Universidad de La Serena, Raul Bitrán 1305, La Serena 2204000, Chile
[35] Departamento de Astronomía, Universidad de La Serena, Av. Juan Cisternas 1200 Norte, La Serena 1720236, Chile
[36] Department of Physics, University of the Pacific, Stockton, CA 90340, USA
[37] Department of Astronomy, University of Michigan, 1085 S. University Ave, Ann Arbor, MI 48109-1107, USA
[38] European Space Agency, ESA/ESTEC, Keplerlaan 1, 2201 AZ Noordwijk, The Netherlands
[39] Dipartimento di Fisica e Astronomia "G.Galilei," Universitá di Padova, Via Marzolo 8, I-35131 Padova, Italy
[40] Departamento de Física Teórica, Atómica y Óptica, Universidad de Valladolid, E-47011 Valladolid, Spain
[41] Instituto de Astrofísica e Ciências do Espaço, Universidade de Lisboa, OAL, Tapada da Ajuda, PT1349-018 Lisbon, Portugal
[42] Osservatorio Astronomico di Roma, via Frascati 33, Monte Porzio Catone, Italy
[43] School of Earth and Space Exploration, Arizona State University, Tempe, AZ 85287, USA
[44] AAAS S&T Policy Fellow hosted at the National Science Foundation, 1200 New York Avenue, NW, Washington, DC 20005, USA
[45] Department of Physics & Astronomy, University of California, Irvine, 4129 Reines Hall, Irvine, CA 92697, USA
[46] Centre for Astrophysics & Supercomputing, Swinburne University of Technology, Hawthorn, VIC 3122, Australia
[47] ARC Centre of Excellence for All Sky Astrophysics in 3 Dimensions (ASTRO 3D), Australia
[48] Institute for Astronomy, University of Edinburgh, Blackford Hill, Edinburgh EH9 3HJ, UK
[49] Department of Physics and Astronomy, University of the Western Cape, Robert Sobukwe Road, Bellville, Cape Town 7535, South Africa
[50] Department of Physics and Astronomy, Johns Hopkins University, 3400 N. Charles Street, Baltimore, MD 21218, USA
[51] Racah Institute of Physics, The Hebrew University of Jerusalem, Jerusalem 91904, Israel
[52] Department of Astronomy & Physics, Saint Mary's University, 923 Robie Street, Halifax, NS B3H 3C3, Canada
[53] Université de Strasbourg, CNRS, Observatoire Astronomique de Strasbourg, UMR 7550, F-67000 Strasbourg, France
[54] Cosmic Dawn Center (DAWN), Jagtvej 128, DK-2200 Copenhagen N, Denmark
[55] Niels Bohr Institute, University of Copenhagen, Lyngbyvej 2, DK-2100 Copenhagen Ø, Denmark
[56] Departamento de Física de la Tierra y Astrofísica, Facultad de CC Físicas, Universidad Complutense de Madrid, E-28040 Madrid, Spain
[57] Instituto de Física de Partículas y del Cosmos IPARCOS, Facultad de CC Físicas, Universidad Complutense de Madrid, E-28040 Madrid, Spain
[58] Department of Physics and Astronomy, Rutgers, the State University of New Jersey, Piscataway, NJ 08854, USA
[59] Université Paris-Saclay, Université Paris Cité, CEA, CNRS, AIM, F-91191 Gif-sur-Yvette, France
[60] Shawnee State University, Portsmouth, OH, USA
[61] Physics & Astronomy Department, University of Louisville, Louisville, KY 40292, USA
[62] Institute of Physics, Laboratory of Galaxy Evolution, Ecole Polytechnique Fédérale de Lausanne (EPFL), Observatoire de Sauverny, 1290 Versoix, Switzerland
[63] Instituto de Astrofísica de Canarias, La Laguna, Tenerife, Spain
[64] Universidad de la Laguna, La Laguna, Tenerife, Spain
[65] Université Paris Cité, LERMA—Observatoire de Paris, PSL, Paris, France
[66] Dunlap Institute for Astronomy & Astrophysics, University of Toronto, Toronto, ON M5S 3H4, Canada
[67] Department of Astronomy, Williams College, Williamstown, MA 01267, USA
[68] NSF's NOIRLab, 950 N. Cherry Avennue, Tucson, AZ 85719, USA
[69] Department of Physics, The Catholic University of America, Washington, DC 20064, USA
[70] Center for Research and Exploration in Space Science and Technology, NASA/GSFC, Greenbelt, MD 20771, USA
[71] Observational Cosmology Laboratory, Code 665, NASA Goddard Space Flight Center, Greenbelt, MD 20771, USA
[72] Minnesota Institute for Astrophysics, University of Minnesota, 116 Church Street SE, Minneapolis, MN 55455, USA
[73] Division of Energy, Matter and Systems, School of Science and Engineering, University of Missouri–Kansas City, Kansas City, MO 64110, USA
[74] Department of Physics and Astronomy, University of California, Riverside, 900 University Avenue, Riverside, CA 92521, USA
[75] Department of Physics and Astronomy and PITT PACC, University of Pittsburgh, Pittsburgh, PA 15260, USA
[76] Research School of Astronomy and Astrophysics, Australian National University, Canberra, ACT 2600, Australia
[77] Columbia Astrophysics Laboratory, Columbia University, 550 West 120th Street, New York, NY 10027, USA
[78] Department of Physics and Astronomy, University of California, Davis, One Shields Ave, Davis, CA 95616, USA
[79] CAS Key Laboratory for Research in Galaxies and Cosmology, Department of Astronomy, University of Science and Technology of China, Hefei 230026, People's Republic of China
[80] School of Astronomy and Space Sciences, University of Science and Technology of China, Hefei, 230026, People's Republic of China
[81] Department of Physics, University of Warwick, Coventry CV4 7AL, UK
[82] IPAC, Mail Code 314-6, California Institute of Technology, 1200 E. California Boulevard, Pasadena, CA 91125, USA
[83] MMT/Steward Observatory, University of Arizona, 933 N. Cherry Avenue, Tucson, AZ 85721, USA
[84] Steward Observatory, University of Arizona, 933 N. Cherry Avenue, Tucson, AZ 85721, USA
[85] Department of Physics, University of Bath, Claverton Down, Bath BA2 7AY, UK
Received 2022 August 2; revised 2022 December 1; accepted 2022 December 13; published 2023 January 25

Abstract

Lyman-break galaxy (LBG) candidates at $z \gtrsim 10$ are rapidly being identified in James Webb Space Telescope (JWST)/NIRCam observations. Due to the (redshifted) break produced by neutral hydrogen absorption of rest-frame UV photons, these sources are expected to drop out in the bluer filters while being well detected in redder filters. However, here we show that dust-enshrouded star-forming galaxies at lower redshifts ($z \lesssim 7$) may also mimic the near-infrared (near-IR) colors of $z > 10$ LBGs, representing potential contaminants in LBG candidate samples. First, we analyze CEERS-DSFG-1, a NIRCam dropout undetected in the F115W and F150W filters but detected at longer wavelengths. Combining the JWST data with (sub)millimeter constraints, including deep NOEMA interferometric observations, we show that this source is a dusty star-forming galaxy (DSFG) at $z \approx 5.1$. We also present a tentative 2.6σ SCUBA-2 detection at 850 μm around a recently identified $z \approx 16$ LBG candidate in the same field and show that, if the emission is real and associated with this candidate, the available photometry is consistent with a $z \sim 5$ dusty galaxy with strong nebular emission lines despite its blue near-IR colors. Further

observations on this candidate are imperative to mitigate the low confidence of this tentative submillimeter emission and its positional uncertainty. Our analysis shows that robust (sub)millimeter detections of NIRCam dropout galaxies likely imply $z \sim 4$–6 redshift solutions, where the observed near-IR break would be the result of a strong rest-frame optical Balmer break combined with high dust attenuation and strong nebular line emission, rather than the rest-frame UV Lyman break. This provides evidence that DSFGs may contaminate searches for ultra-high redshift LBG candidates from JWST observations.

Unified Astronomy Thesaurus concepts: High-redshift galaxies (734); Galaxies (573); Lyman-break galaxies (979); Galaxy photometry (611); Submillimeter astronomy (1647); Millimeter astronomy (1061); Luminous infrared galaxies (946); Starburst galaxies (1570); James Webb Space Telescope (2291); Near infrared astronomy (1093); Dust continuum emission (412); Emission line galaxies (459)

1. Introduction

The superb sensitivity of the James Webb Space Telescope (JWST) coupled with its high angular resolution and its near-infrared (near-IR) detectors (Rigby et al. 2022) provides a unique view of the universe previously invisible to other telescopes, from nearby star-forming regions to the farthest, faintest galaxies ever found. In the field of extragalactic astronomy, JWST allows us to extend the Lyman-break galaxy (LBG) selection technique beyond $z \gtrsim 11$, the redshift at which the Lyman break is redshifted beyond the reach of Hubble Space Telescope (HST) coverage (Hubble serving as the previous workhorse instrument for the identification of such galaxies before the arrival of JWST; see reviews by Finkelstein 2016; Stark 2016; Robertson 2022 and references therein).

The identification of very high-redshift LBGs has strong implications for our understanding of galaxy formation and evolution. For example, the confirmation of large numbers of $z > 11$ galaxies can provide strong constraints on the formation epoch of the first galaxies and their star formation efficiencies. Their existence can shed light on the dark matter halo mass function in the early universe, particularly with the presence of very luminous sources found $\lesssim$400 Myr after the Big Bang (e.g., Behroozi et al. 2019).

In the first few days after the release of the first JWST observations, an increasing number of samples of LBG candidates at $z \gtrsim 10$ were identified (Adams et al. 2023; Atek et al. 2023; Castellano et al. 2022; Donnan et al. 2023; Finkelstein et al. 2022a; Harikane et al. 2022; Naidu et al. 2022; Yan et al. 2023). The abundance and masses of these sources start to be in tension with the predictions from most galaxy formation models (Boylan-Kolchin 2022; Finkelstein et al. 2022a; Lovell et al. 2023). Nevertheless, the observed colors for some of these very high-redshift candidates may be degenerated with other populations of galaxies at lower redshifts. This results from confusion between the Lyα forest break at $z > 12$ with the Balmer and the 4000 Å breaks combined with dust attenuation and/or strong nebular emission. This means that dusty star-forming galaxies (DSFGs) at significantly lower redshifts ($z \lesssim$ 6–7) can mimic the JWST/NIRCam colors of $z \gtrsim 10$ LBGs, particularly in the shortest-wavelength filters. While models tend to assume these galaxies are universally red in color, thus distinguishable from the typically very blue LBGs, the complex environments of the interstellar medium (ISM) within DSFGs plus contamination from nebular emission lines could lead to a mix of observed near-IR colors (Howell et al. 2010; Casey et al. 2014b), further obfuscating the secure identification of ultra-high redshift LBGs. The phenomenon of DSFGs contaminating high-redshift LBG searches is, in fact, not new to JWST, as often $z \sim 2$–3 DSFGs were found to contaminate $z \sim 6$–8 LBG samples selected by HST (e.g., Dunlop et al. 2007); here, both the contaminants (DSFGs at $z \sim 4$–6) and LBG targets ($z \sim 10$–20) for JWST have shifted to higher redshifts.

The secure identification of LBGs is thus important not only to quantify the contamination fraction in $z \gtrsim 10$ LBG samples (which could relax the observed tension between observations and model predictions) but also to constrain the volume density and physical properties of early massive quiescent galaxies and high-redshift DSFGs, an important step toward our ultimate goal of understanding galaxy formation and evolution. However, distinguishing these galaxies from other populations has proven challenging and requires spectroscopic or multiwavelength observations probing the older stellar populations (for the quiescent systems) or the dust thermal emission (for DSFGs).

Here, we use JCMT/SCUBA-2 850 μm and NOEMA 1.1 mm interferometric observations, in combination with the JWST data from the Cosmic Evolution Early Release Science (CEERS) Survey (Finkelstein et al. 2017; Bagley et al. 2022; S. Finkelstein et al. 2022, in preparation), to search for dust emission around $z > 12$ galaxy candidates and NIRCam dropout sources. We report on a galaxy, CEERS-DSFG-1, that is undetected in the NIRCam F115W and F150W filters, but whose photometric redshift is well constrained to be around $z = 5$ after including (sub)millimeter data. We also study the $z \sim 16.7$ candidate, CEERS-93316, reported in Donnan et al. (2023), for which we find a tentative 2.6σ detection at 850 μm, and show that, if this emission is real and associated with this source, it would imply a lower-redshift solution around $z \sim 5$. Finally, we examine all the available long-wavelength (mid-IR to millimeter) observations around the $z \approx 12$ candidate known as Maisie's galaxy (Finkelstein et al. 2022a), finding no evidence of continuum emission.

This Letter is organized as follows: Section 2 describes the new observations and the ancillary data sets. In Section 3 we describe the spectral energy distribution (SED) fitting methodology and the best-fit SED fitting for CEERS-DSFG-1 along with the inferred physical properties. Then, Section 4 introduces our search for potential contamination from other DSFGs in samples of $z > 12$ LBGs candidates in the CEERS field including CEERS-93316 and Maisie's galaxy. Finally, our conclusions are summarized in Section 5.

In this Letter, we assume $H_0 = 67.3\,\mathrm{km\,s^{-1}\,Mpc^{-1}}$, $\Omega_\lambda = 0.68$, and $\Omega_\mathrm{M} = 0.32$ (Planck Collaboration et al. 2016).

2. Observations

2.1. NOEMA Observations

We obtained NOEMA continuum observations on a sample of 19 DSFG candidates in the Extended Groth Strip (EGS) field in preparation for CEERS JWST data, as part of the NOEMA

Program W20CK (PIs: Buat and Zavala). The targets were selected from the original sample reported in Zavala et al. (2017, 2018b) based on deep observations at both 450 and 850 μm obtained with the SCUBA-2 camera on the James Clerk Maxwell Telescope (JCMT). Here, we only focus on CEERS-DSFG-1 (known as 850.027 in Zavala et al. 2017, 2018b). The rest of the observations, along with a detailed description of the sample selection, will be presented elsewhere (L. Ciesla et al. 2022, in preparation).

NOEMA observations were performed using the wideband correlator *Polyfix* covering the frequency ranges 252.5–260 GHz (with the lower side band) and 268–275.5 GHz (with the upper side band). The on-source integration time varies from ∼10 to ∼50 minutes and was determined based on the 850 μm flux densities of each target. For the main target of this Letter, CEERS-DSFG-1, the on-source integration time was around 25 minutes. Calibration and imaging of the *uv* visibilities were then performed with GILDAS,[86] producing continuum maps with $0\farcs15 \times 0\farcs15$ pixels centered at 270 GHz. For CEERS-DSFG-1, the achieved rms is measured to be $\sigma_{1.1\,\mathrm{mm}} = 0.10$ mJy beam^{-1}, and the beam size is $1\farcs35 \times 0\farcs85$. The continuum flux density at 1.1 mm was extracted using an aperture of 1.5× the beam size to recover any potential extended emission resolved by the beam.

Our NOEMA observations did not explicitly target the other two sources we include in this Letter, CEERS-93316 or Maisie's galaxy, although the former is covered in a low sensitivity, outlying part of the primary beam of the observations of CEERS-DSFG-1. We discuss this further in Section 4.

2.2. CEERS Data

JWST/NIRCam observations were conducted as part of the CEERS (S. Finkelstein et al. 2022, in preparation) Survey program, one of the early release science surveys (Finkelstein et al. 2017). Here, we only use data from CEERS pointing #2, which covers all three objects we study in seven filters: F115W, F150W, F200W, F277W, F356W, F410M, and F444W. After a three-dither pattern, the total exposure time was typically 47 minutes per filter, with the exception of F115W, whose integration time is longer (see details in Finkelstein et al. 2022a and S. Finkelstein 2022, in preparation).

We performed a detailed reduction as described in Bagley et al. (2022) and Finkelstein et al. (2022b). What follows is a brief summary of the main steps, and we refer the reader to these two papers for more details. We used version 1.7.2 of the JWST Calibration Pipeline,[87] with custom modifications. Raw images were processed through Stages 1 and 2 of the pipeline, which apply detector-level corrections, flat-fielding, and photometric flux calibration. We also applied a custom step to measure and remove $1/f$ noise. We align the F200W images to an HST/WFC3 F160W reference catalog created from $0\farcs03$ pixel^{-1} mosaics in the EGS field with astrometry tied to Gaia-EDR3 (see Koekemoer et al. 2011 for more details about the methodology). We then aligned each NIRCam filter to F200W, achieving a median astrometric offset $\lesssim 0\farcs005$. Our steps represent an initial reduction that will be iteratively improved with updates to the Calibration Pipeline and reference files.

[86] www.iram.fr/IRAMFR/GILDAS
[87] jwst-pipeline.readthedocs.io

The flux extraction was done following S. Finkelstein et al. (2022, in preparation). Briefly, we use a multiwavelength photometric catalog created with Source Extractor (Bertin & Arnouts 1996), that was created with a sum of F277W+F356W as the detection image, with colors measured in small Kron apertures on images PSF-matched to F444W. Total fluxes were estimated following an aperture correction based on a ratio between a large Kron (MAG_AUTO) flux and the small Kron flux in the F444W image, with an additional correction for missing light in the large aperture based on simulations. Finally, a systematic offset of 1%–5% was applied based on comparing the colors of best-fitting model templates to the photometry for ∼800 spectroscopically confirmed galaxies.

2.3. Other Ancillary Data

Photometric constraints at 450 and 850 μm were obtained from Zavala et al. (2017), who reported deep observations with a central depth of $\sigma_{450\,\mu\mathrm{m}} = 1.2$ mJy beam^{-1} and $\sigma_{850\,\mu\mathrm{m}} = 0.2$ mJy beam^{-1}, respectively, with a beam size of $\theta_{450\,\mu\mathrm{m}} \approx 8''$ and $\theta_{850\,\mu\mathrm{m}} \approx 14\farcs5$.

We also make use of Spitzer IRAC 8 μm (Barro et al. 2011) and MIPS 24 μm (Magnelli et al. 2009) observations, as well as Herschel photometry from PACS (at 100 and 160 μm; Lutz et al. 2011) and SPIRE (at 250, 350, and 500 μm; Oliver et al. 2012). Note, however, that the sources studied here are not detected in the Spitzer or Herschel maps and so we adopt only upper limits. In addition, we use a 3 GHz mosaic of the EGS field (M. Dickinson 2022, private communication) obtained using observations from the Karl G. Jansky Very Large Array (VLA) as part of the program 21B-292 (PI: M. Dickinson). It reaches a sensitivity of 1.5 μJy beam^{-1} and angular resolution of $2\farcs3 \times 2\farcs3$.

The photometry extracted from these observations is summarized in Table 1.

3. A JWST/NIRCam Dropout: A DSFG at Redshift Five

The subarcsecond positional accuracy of the NOEMA observations allows us to directly identify the submillimeter-selected galaxy, CEERS-DSFG-1, in the JWST/NIRCam observations (see Figure 1) without any ambiguity. Interestingly, CEERS-DSFG-1 is well detected in F200W and redder bands but abruptly drops out in F150W and F115W and in all the HST filters, as can be seen in Figure 2. The dropout nature of this source satisfies some of the color criteria to identify $z > 10$ galaxy candidates. Indeed, it satisfies the criterion of $m_{150\mathrm{W}} - m_{200\mathrm{W}} > 0.8$ used in Yan et al. (2023), and some (but not all) of the criteria used in Donnan et al. (2023), with a 2σ nondetection in F115W and F150W, and $>3\sigma$ detections in redder filters (see Figure 2 and Table 1). However, the identification of this source as a DSFG calls into question such a very high-redshift scenario, given that the highest-redshift dust continuum detections ever reported are at $z \sim 7$–8 (Laporte et al. 2017; Strandet et al. 2017; Marrone et al. 2018; Tamura et al. 2019; Inami et al. 2022). Moreover, the (sub)millimeter emission would imply an extreme infrared (IR) luminosity in excess of $\sim 10^{13}\,L_{\odot}$ and a large dust mass in tension with current models. This is thoroughly discussed in Appendix A, where we show that relatively bright (sub)millimeter sources are unlikely to lie at $z > 10$.

Table 1
Measured Photometry of CEERS-DSFG-1

Instrument/Filter	Wavelength	Flux Density
NIRCam/F115W	1.15 μm	-8 ± 11 nJy
NIRCam/F150W	1.50 μm	18 ± 13 nJy
NIRCam/F200W	2.00 μm	41 ± 13 nJy
NIRCam/F277W	2.77 μm	137 ± 8 nJy
NIRCam/F356W	3.56 μm	259 ± 8 nJy
NIRCam/F410M	4.10 μm	420 ± 15 nJy
NIRCam/F444W	4.44 μm	438 ± 12 nJy
PACS/100 μm	100 μm	0.11 ± 0.51 mJy
PACS/160 μm	160 μm	0.1 ± 3.5 mJy
SPIRE/250 μm	250 μm	-1.1 ± 5.8 mJy
SPIRE/350 μm	350 μm	-4.5 ± 6.3 mJy
SCUBA-2/450 μm	450 μm	-2.5 ± 1.7 mJy
SPIRE/500 μm	500 μm	-1.0 ± 6.8 mJy
SCUBA-2/850 μm	850 μm	2.25 ± 0.36 mJy
NOEMA/1.1 mm	1.1 mm	1.92 ± 0.11 mJy

Note. AB magnitudes can be derived via $-2.5 \log_{10}(f_\nu\,[\mathrm{nJy}]) + 31.4$. CEERS-DSFG-1 is formally not detected in F115W, all of the Herschel bands from 100 to 500 μm, and SCUBA-2 450 μm.

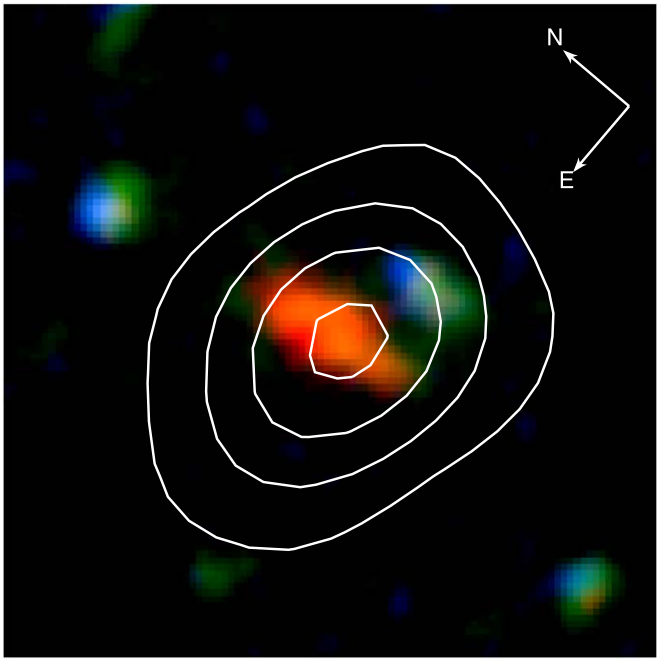

Figure 1. A $3\farcs0 \times 3\farcs0$ composite image centered at the position of CEERS-DSFG-1; the JWST/NIRCam F115W observations are in blue, F277W in green, and F444W in red (the data have been smoothed to roughly match the F444W resolution for better visualization). The 1.1 mm NOEMA signal-to-noise ratio levels starting at 2.5σ to 10σ (in steps of 2.5σ) are represented by the white contours, clearly indicating that the dust thermal emission detected at submillimeter/millimeter wavelengths corresponds to the position of CEERS-DSFG-1.

Here we conduct a more thorough investigation as to the possible redshift of CEERS-DSFG-1 using JWST constraints alone, (sub)millimeter constraints alone, and a combination of both JWST and long-wavelength millimeter data. The results are highly dependent on the available photometric constraints and the inferred redshifts differ significantly, as discussed below in this section.

3.1. SED Fitting Procedure and Redshift Constraints

3.1.1. EAZY

We first fit the SED of CEERS-DSFG-1 to JWST/NIRCam photometry alone using the EAZY (Brammer et al. 2008) SED fitting code. The fitting was performed in an identical fashion as in Finkelstein et al. (2022a). To summarize, EAZY makes use of a user-supplied template set to generate linear combinations of stellar populations that fit the data and generate redshift probability distributions. The template set used in our case includes the "tweak_fsps_QSF_12_v3" set of 12 templates as well as 6 additional templates that span bluer colors (Larson et al. 2022). As shown in Figure 3, the redshift probability density distribution from EAZY shows two significant peaks at $z \sim 3$ and $z \sim 5$, and a nonnegligible probability ($\sim$6%) at $z \approx 12$–14. To put these fits in context with the (sub)millimeter data, we show in Figure 4 the best-fit SED from EAZY at $z = 5.5$, corresponding to the redshift with the maximum probability.

3.1.2. CIGALE

We also fit the photometry using CIGALE (Burgarella et al. 2005; Noll et al. 2009; Boquien et al. 2019) assuming a delayed star formation history (SFH): $\mathrm{SFR}(t) \propto t \exp(-t/\tau)$ with stellar models from Bruzual & Charlot (2003). A Calzetti et al. (2000) law is also adopted for the dust attenuation of the stellar continuum. On the other hand, the nebular emission (continuum and lines) is attenuated with a screen model and an small magellanic cloud-like extinction curve (Pei 1992). Finally, the dust emission reemitted in IR is modeled with Draine et al. (2014) models.

Including only JWST/NIRCAM photometry in the fit results in a similar redshift distribution as the one obtained with EAZY, with significant probability at $z \approx 3$–5 and a moderate probability of $\approx$22% of being at $z > 10$. To illustrate how well the high-redshift solutions fit the available data, we include the best-fit SED at $z = 13.5$ in Figure 4.

In addition, we fit the JWST data along with SCUBA-2 and NOEMA detections (Herschel upper limits were not included in the fit) using the same CIGALE configuration described above. The addition of the long-wavelength data significantly impacts the results, narrowing down the redshift probability distribution of CEERS-DSFG-1 (see Figure 3). The best-fit photometric redshift when using all the available photometric constraints is $z = 5.09^{+0.62}_{-0.72}$, where the error bars encompass the 68% confidence interval. As shown in Figure 4, the fitted SED from this analysis is in good agreement with all the available photometric constraints, including upper limits.

3.1.3. MMPz

Finally, though the long-wavelength data on CEERS-DSFG-1 are somewhat limited, we are able to calculate an independent photometric redshift for the source based on long-wavelength data alone using the MMPZ package (Casey 2020). MMPZ presumes that sources with significant (sub)millimeter emission follow an empirically measured relationship between the rest-frame peak wavelength of emission, λ_{peak}, which is inversely proportional to the characteristic luminosity-weighted dust temperature of the ISM, and the total emergent IR luminosity,

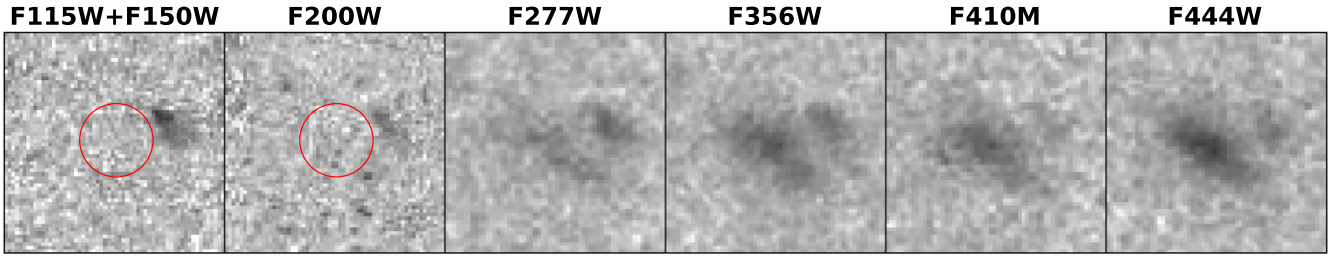

Figure 2. $1\farcs8 \times 1\farcs8$ cutouts around CEERS-DSFG-1 from the CEERS JWST/NIRCam bands. The source is undetected in F115W, F150W, and F200W (the source's position is indicated with the red circle in the stacked F115W+F150W and F200W images, the dropout bands). The galaxy is well detected in redder filters with a red spectral shape. All images follow the same color code with a maximum value equal to 15× the sky rms and a minimum value of -1.5σ and have the same orientation as Figure 1.

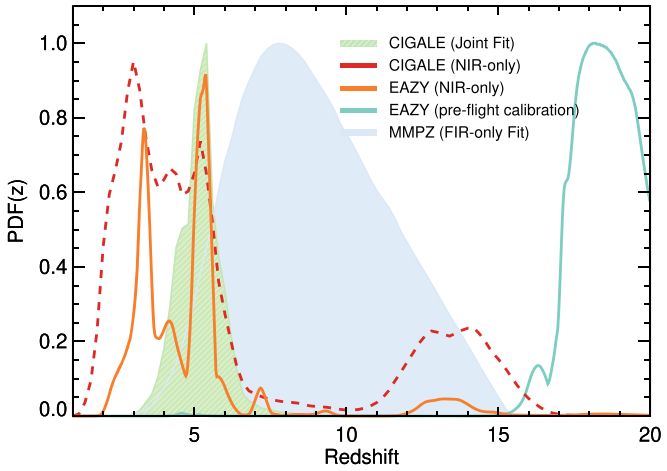

Figure 3. Normalized redshift probability density distributions for CEERS-DSFG-1 from the different SED fittings. The broad solid light blue distribution centered at $z \sim 7.7$ comes from the (sub)millimeter wavelength constraints using MMPZ (Casey 2020). The fits to the JWST photometry alone from EAZY (orange) and CIGALE (red) are also very uncertain and show nonnegligible probabilities at several very different redshift ranges. On the other hand, the joint CIGALE fit to the NIRCam and the (sub)millimeter data results in a narrow distribution, constraining the redshift of CEERS-DSFG-1 at $z = 5.09^{+0.62}_{-0.72}$. Finally, to illustrate the impact of preflight NIRCam calibrations on the redshifts constraints, we also show the results from an EAZY fit to previous reductions of the NIRCam imaging (cyan line), which pushed the redshift constraints at $z > 15$.

$L_{\rm IR}$. This $L_{\rm IR}$–$\lambda_{\rm peak}$ relation is fairly well constrained out to $z \sim 5$ (Casey et al. 2018; Drew & Casey 2022) where more intrinsically luminous sources have warmer temperatures. MMPZ generates a redshift probability distribution by computing the $L_{\rm IR}$ and $\lambda_{\rm peak}$ at all possible redshifts, and contrasts that against the empirical distribution of measured SEDs. By design, redshift solutions found using MMPZ are very broad (due to the degeneracy between ISM dust temperature, constrained via $\lambda_{\rm peak}$, and redshift). The best-fit redshift generated from the long-wavelength data alone (including the only two detections and all the nondetections) is most consistent with the joint CIGALE fit, but shifted to higher values with a best-fit redshift of $z = 7.77^{+2.55}_{-1.69}$ (see Figure 3).

3.1.4. The Moral of the Story

From the above analysis, it is clear that a single color (i.e., dropout) selection criteria to identify high-redshift ($z \gtrsim 10$) candidates might include contamination from lower-redshift sources, such as CEERS-DSFG-1. This contamination could be more severe in studies using preflight calibrations since they render the colors of some galaxies more akin to those expected for very high-redshift systems (see discussion by Adams et al. 2023). This is clearly illustrated in Figure 3, where we have also included the photometric redshift constraints from EAZY using a preflight calibration. The fit suggests a very high redshift of $z = 18.2^{+1.2}_{-0.7}$ with an almost negligible probability at $z < 15$. Careful selection criteria (with several conditions) are thus necessary to produce cleaner samples of high-redshift galaxies. Finkelstein et al. (2022b) and Harikane et al. (2022), for example, implemented a further criterion based on the significance of the high-redshift solution against secondary lower-redshift solutions (defined by the difference between the χ^2 values of the high-redshift and low-redshift solutions) to select robust candidates (see also Donnan et al. 2023). Similarly, other studies used a two-color criterion to minimize contaminants (e.g., Adams et al. 2023; Atek et al. 2023; Castellano et al. 2022; Harikane et al. 2022) that would have prevented the selection of CEERS-DSFG-1 as a very high-redshift candidate given its red colors at longer wavelengths (e.g., $m_{277\rm W} - m_{444\rm W} > 1.26$). Note, however, that despite these extra selection criteria, lower-redshift systems might still masquerade (and be misidentified) as very high-redshift galaxies as discussed in Section 4.

3.2. On the Physical Properties of CEERS-DSFG-1

As mentioned above, the joint fit of CIGALE using the JWST/NIRCam and the (sub)millimeter data provide tight constraints on the redshift of our target and its physical properties. Hence, here we adopt the these results as our fiducial values. The inferred physical properties are summarized in Table 2 and discussed below.

Assuming the best-fit redshift of $z = 5.1$, the stellar mass of CEERS-DSFG-1 is constrained to be $(2.1 \pm 0.8) \times 10^{10} M_\odot$. This is a factor of ∼4 smaller than the average mass of DSFGs detected by single-dish telescopes (e.g., da Cunha et al. 2015), but is aligned with expectations since our source was selected from one of the deepest SCUBA-2 850 μm surveys and has a fainter 850 μm flux density than typical galaxies identified in shallower single-dish telescope surveys. Indeed, the stellar mass of our target is in better agreement with other SCUBA-2 galaxies identified in this field, which have an average stellar mass of $\approx 5.6 \times 10^{10} M_\odot$ (Cardona-Torres et al. 2022), and with the masses derived for galaxies identified in recent deeper Atacama Large Millimeter/submillimeter Array (ALMA) surveys (e.g., Gómez-Guijarro et al. 2022; see also Khusanova et al. 2021). Similarly, the star formation rate (SFR) of CEERS-DSFG-1 of $110 \pm 30\, M_\odot\, yr^{-1}$ (averaged over the past 10 Myr) lie between those from submillimeter galaxies (SMGs) and fainter DSFGs identified in deeper ALMA observations

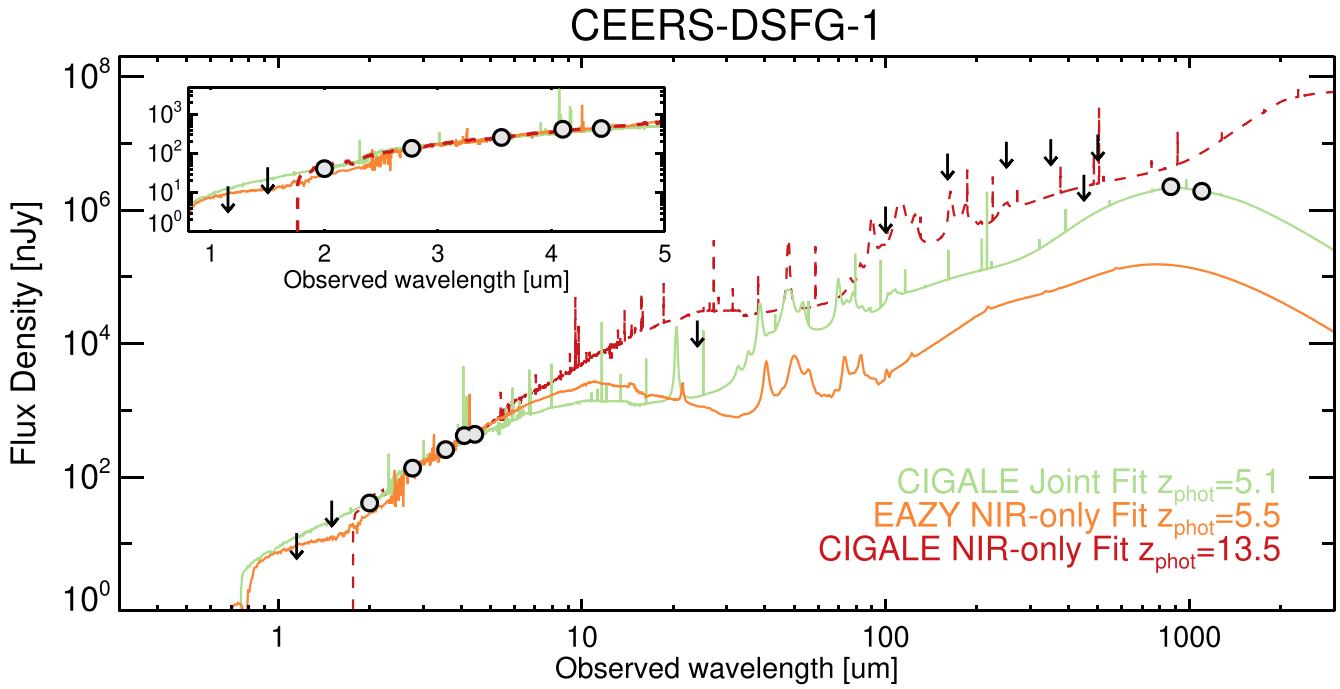

Figure 4. The full near-infrared through millimeter spectral energy distribution of CEERS-DSFG-1 overplotted with several of the best-fit SEDs described in Section 3 along with the current photometric constraints. The detections used in the fits are represented by the solid circles, while 2σ upper limits are illustrated by the downward arrows (note that error bars are smaller than the symbols). We show the EAZY fit to near-IR data only at $z = 5.5$ in orange, CIGALE to near-IR data only at $z = 13.5$ in red, and the fiducial CIGALE joint fit at $z = 5.1$ in light green. While the three SEDs satisfactorily reproduce the JWST photometry (see zoom-in inset plot), only the joint fit at $z = 5.1$ reproduces the (sub)millimeter fluxes.

Table 2
Properties of CEERS-DSFG-1

Property	Value
Source ID	CEERSJ141938.19+525613.9
R.A. (J2000 [deg])	214.9091152
Decl. (J2000 [deg])	52.9371977
$z_{\rm CIGALE}$	$5.09^{+0.62}_{-0.72}$
$M_\star$ ($M_\odot$)	$(2.1 \pm 0.8) \times 10^{10}$
$L_{\rm IR}$ ($L_\odot$)	$(1.1 \pm 0.3) \times 10^{12}$
SFR ($M_\odot$ yr^{-1})	110 ± 30
sSFR (Gyr^{-1})	5.2 ± 2.5
$E(B-V)$ (mag)	1.6 ± 0.1
Age (Myr)	490 ± 240
Mass-weighted age (Myr)	170 ± 90

Note. The redshift and the listed physical properties were derived from the joint fit of CIGALE using the JWST/NIRCam data and the available (sub) millimeter constraints.

(da Cunha et al. 2015; Zavala et al. 2018a; Aravena et al. 2020; Casey et al. 2021; Khusanova et al. 2021; Gómez-Guijarro et al. 2022). These properties imply a specific star formation rate of sSFR $= 5.2 \pm 2.5$ Gyr^{-1}, meaning that CEERS-DSFG-1 lies on the main sequence of star-forming galaxies, similar to the so-called population of "HST-dark" galaxies[88] (e.g., Wang et al. 2019).

At $z = 5.1$, the NIRCam photometry samples rest-frame wavelengths from 0.2 to 0.7 μm, allowing us to constrain the stellar dust attenuation. The red spectral shape in the NIRCam bands implies a strong dust attenuation (as typically found for this kind of galaxies; e.g., Simpson et al. 2017) with $E(B-V) = 1.6 \pm 0.04$, which results in a dust luminosity of $(1.1 \pm 0.3) \times 10^{12}\, L_\odot$.

[88] CEERS-DSFG-1 is, by definition, an "HST-dark" galaxy.

4. Searching for DSFG Contaminants in High-redshift LBG Candidates Identified with JWST

The SCUBA-2 observations from Zavala et al. (2017) partially overlap with the CEERS NIRCam survey and thus can be used to look for dust continuum emission around $z > 10$ candidates in the field. Here we focus on two recently reported high-redshift candidates: CEERS-93316 reported to be at $z \approx 16.7$ (Donnan et al. 2023) and Maisie's galaxy at $z \approx 11.8$ (Finkelstein et al. 2022a).

4.1. A Deeper Look into CEERS-93316

A 2.6σ tentative detection around the position of CEERS-93316 (Donnan et al. 2023; R.A. = 214.91450, decl. = 52.943033) was found in the 850 μm SCUBA-2 map with a flux density of 0.65 ± 0.26 mJy (see Figure 5). Unfortunately, this source was not formally targeted by our NOEMA observations and, although it is only 26″ away from CEERS-DSFG-1 and within the coverage of the NOEMA map described above, it lies on the edge of the map, where the sensitivity is very low (with a primary beam response of $\lesssim$0.1, implying an rms of $\sigma_{1.1\ \rm mm} \gtrsim 1$ mJy beam^{-1}).

4.1.1. Caveats of a Marginal SCUBA-2 Detection

We emphasize that there are two primary reasons why this marginal detection may not conclusively imply that CEERS-93316 is a significant thermal dust emitter. The first concern is the significance of the signal itself and the possibility of being spurious. At 2.6σ, simulations of blind detections, single-dish submillimeter sources indicate false-positive rates as high as

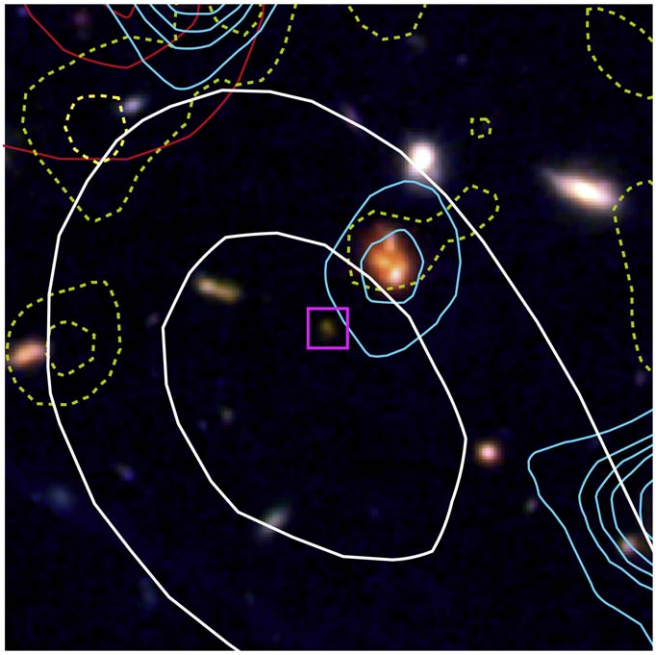

Figure 5. A $12\farcs0 \times 12\farcs0$ composite image (blue: F115W; green: F277W; red: F444W) centered at the position of the $z = 16.7$ candidate from Donnan et al. (2023; magenta square). The deep SCUBA-2 850 μm map from Zavala et al. (2017) shows a $\sim$2.6σ positive emission at this position (white contours indicate 1σ and 2σ levels). We also plot signal-to-noise contours at 1σ, 2σ, 2.5σ, 3σ, and 4σ from Spitzer 8 μm and 24 μm as cyan and red lines, respectively, and from VLA 3 GHz as yellow dashed lines. From the lack of clear detections, we can rule out an obvious alternate radio or 24 μm counterpart for the 850 μm emission at $z \lesssim 3$, while we cannot rule out galaxies at $z \gtrsim 3$ since they are usually undetected at these wavelengths. The marginal 8 μm emitter on the top right (west) of CEERS-93316 is a potential counterpart, but the current data are unconstraining.

$\sim$30%–40% (Casey et al. 2013, 2014a). These rates of false positives are estimated by both searching SCUBA-2 maps for negative significance peaks at -2.6σ as well as conducting source injection tests on SCUBA-2 jackknife maps (following the same methodology as Casey et al. 2013, see their Figure 7). To complement these results, we test the reliability of these low signal-to-noise ratio peaks by creating a catalog of 2.5σ to 3.0σ SCUBA-2 sources and searching for counterparts in the deep VLA 3 GHz map (Dickinson, private communication). We find clear associations for at least 50% of the SCUBA-2 sources,[89] implying a $\sim$50% fidelity rate. A similar result is obtained using the 24 μm map. Note, however, that this reliability fraction of 50% should be considered a lower limit since it is well known that a significant fraction (as high as 30%–40%) of submillimeter sources lack radio or mid-IR counterparts (particularly those at $z > 3$; Chapman et al. 2003; Pope et al. 2006; Barger et al. 2007; Dye et al. 2008). We thus conclude that the 2.6σ SCUBA-2 signal around CEERS-93316 has a $\gtrsim$50% probability of being real.

The second significant concern is that even if the detection is real, the SCUBA-2 beam size is large enough that the 850 μm emission could arise from another galaxy at a close angular separation with CEERS-93316 on the sky. Figure 5 shows the neighboring sources within the beam size of the SCUBA-2 tentative detection, with contours overlaid for Spitzer 8 μm emission, 24 μm emission, and VLA 3 GHz continuum. Unfortunately, there is no secure emitter at these wavelengths to which we can definitively associate the 850 μm emission to unequivocally rule out association with CEERS-93316. Note that the lack of such a counterpart does not imply the tentative SCUBA-2 emission is spurious, since $z > 3$ galaxies are usually undetected in these bands (this is indeed the case for CEERS-DSFG-1). This lack of detection rather means that it is not implausible to associate the 850 μm emission with CEERS-93316, although it also does not confirm the association. Another possible counterpart could be the 8 μm emitter (with a $\sim$2.5σ significance) to the northwest that has a photometric redshift of $z \sim 5$, though it is farther from the signal-to-noise peak in the SCUBA-2 map than CEERS-93316.

At present, we lack sufficient data to clearly associate the emission with CEERS-93316 or other neighboring sources. Follow-up interferometric observations would be necessary to provide both a confirmation of the emission and astrometric localization to CEERS-93316 or to a neighboring source. Nevertheless, given the remarkable properties of CEERS-93316 (being one of the highest-redshift candidates ever reported with a bright UV magnitude of $M_{\rm UV} = -21.7$), below we explore the impact that the submillimeter tentative detection might have on its redshift solution *if* the dust emission is real *and* associated with it.

4.1.2. Implications if Dust Emission Is Associated with CEERS-93316

First, we consider what the implications would be if CEERS-93316 had significant dust emission at its proposed redshift of $z = 16.7$. The observed 850 μm emission would probe the rest-frame $\sim$50 μm regime; in this scenario, the IR luminosity would be above $10^{12}\,L_{\odot}$ with a dust mass of $\sim 10^{8}\,M_{\odot}$. A system with such high dust mass found $\sim$230 Myr after the Big Bang would surely be extraordinary, likely implausibly so (e.g., Dwek et al. 2014). This is further discussed in Appendix A, where we show the predicted IR luminosity and dust mass as a function of redshift for a hypothetical submillimeter detection with a flux density similar to that of the tentative emission discussed here.

We alternatively explore if a lower-redshift solution would be plausible given the JWST/NIRCam photometric constraints and the observed blue colors in these bands (which contrasts with those from CEERS-DSFG-1). To do that, we fit the JWST/NIRCam data[90] along with the tentative 850 μm flux density with CIGALE.

While the redshift distribution from this fitting strongly favors a high-redshift solution in agreement with the Donnan et al. (2023) result (with $z_{\rm CIGALE} \approx 16.4$; see Figure 6), the best-fit SED does not satisfactorily reproduce the tentative submillimeter flux density that is underestimated by more than 1 order of magnitude (see Figure 7). Interestingly, the redshift probability distribution does show a secondary peak at $z \sim 4.8$, although with a low integrated probability of less than 3% (see Figure 6). This peak is seen even without the inclusion of the long-wavelength emission and it is also seen in the redshift probability density distribution presented by Donnan et al. (2023, see their Figure A1). This lower redshift clearly dominates the probability distribution of the EAZY fitting

[89] Given the surface density of radio and the SCUBA-2 sources, the probability of chance alignment is <5%.

[90] Note that since we performed our own data reduction and followed our own source extraction procedure designed to measure accurate colors, the NIRCam fluxes for CEERS-93316 used in this Letter could differ from those in Donnan et al. (2023). We list the adopted fluxes for the SED fitting in Appendix B.

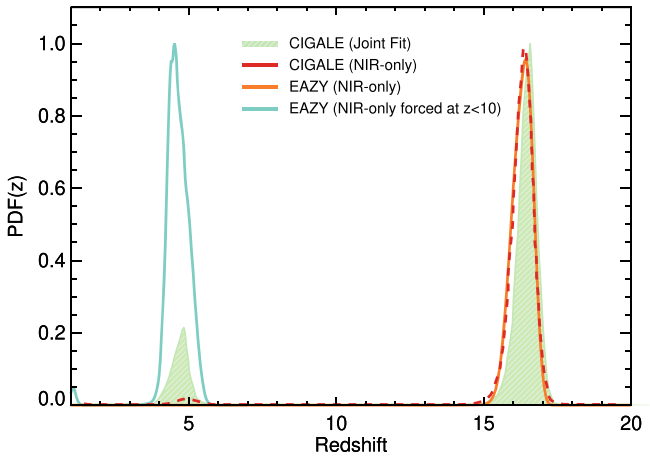

Figure 6. Normalized redshift probability density distributions for CEERS-93316 from the different SED fittings. The EAZY and CIGALE fits to the JWST photometry alone are represented by the orange and red lines, respectively. The two fits suggest a high redshift around ∼16.3, in agreement with Donnan et al. (2023). The addition of the tentative submillimeter emission to the CIGALE fit does not alter the main peak of the distribution, although it increases the probability at $z \sim 4.8$ as illustrated by the green shaded area. This lower-redshift solution is in good agreement with the results from EAZY when imposing a maximum redshift at $z = 10$ (cyan line). As thoroughly discussed in the main text, if the tentative 850 μm emission is real and associated with CEERS-93316, our analysis suggests that this high-redshift galaxy candidate rather lies at a lower redshift around $z \sim 4.8$.

when imposing a maximum redshift[91] of $z = 10$, as shown in the Figure 6.

To further explore the feasibility of this alternative redshift solution, we rerun CIGALE but fix the redshift to $z = 4.8$. The resulting SED is shown in Figure 7 along with the best-fit $z \sim 16$ SEDs from EAZY and CIGALE, for comparison. In the low-redshift scenario, the strong break seen between F200W and F277W in CEERS-93316 is attributable to strong [OIII] and Hβ emission in the F277W band (see Figure 7). Similarly, the excess flux in F356W above the continuum, which produces a blue F356W-F410M color, would be attributable to Hα emission. The measured NIRCam photometry would thus require a young starburst with strong nebular line emission to satisfy a $z \sim 4.8$ solution, but this would be within the realm of expectation for an early-stage DSFG in formation at these redshifts.

The $z \approx 4.8$ best-fit SED would imply an SFR averaged over 10 Myr of $20 \pm 10\,M_{\odot}\,\mathrm{yr}^{-1}$ and a stellar mass equal to $(1.4 \pm 0.5) \times 10^{9}\,M_{\odot}$, with a dust attenuation (for both continuum and lines) of $E(B-V) = 0.5 \pm 0.1$ and a dust luminosity of $(1.7 \pm 0.8) \times 10^{11}\,L_{\odot}$. These properties are in broad agreement with those derived for the relatively faint population of $z \sim 7$ dusty galaxies in the REBELS survey (Bouwens et al. 2020; Inami et al. 2022). In addition, the line fluxes required to reproduce the given NIRCam photometry range from $\sim 1 \times 10^{-18}$–1×10^{-17} erg s^{-1} cm^{-2}, which are within the range of those predicted for CEERS-DSFG-1 .

While deep interferometric observations at millimeter wavelengths are required to confirm or refute dust continuum emission in this high-redshift candidate, here we show (see also Appendix A) that a $z \sim 4.8$ scenario associated with a DSFG with strong nebular emission is plausible for CEERS-93316 and highly likely if the submillimeter emission is confirmed, despite its blue near-IR colors that are usually associated with the emission of dust-free systems (e.g., Finkelstein 2016, and references therein). If this lower-redshift solution is true, it would contrast with the low probability of being at $z < 15$ inferred from the different redshift probability distributions shown in Figure 6 (see also Donnan et al. 2023; Finkelstein et al. 2022b). The reason for this low probability might be related to the low significance of the tentative SCUBA-2 detection in the case of CIGALE or with the adopted templates and the fitting approach for EAZY. Interestingly, Pérez-González et al. (2022), who used a novel 2D fitting approach with a new set of SED templates, found a best-fit redshift of 4.59 ± 0.03 for this source (known as nircam2-2159 in Pérez-González et al. 2022) with a low probability of being at $z > 10$.

4.2. A Deeper Look into Maisie's Galaxy

Given that the recently reported $z = 11.8$ galaxy candidate from Finkelstein et al. (2022a) lies close to the two galaxies described above (∼78″ and ∼65″ away from CEERS-DSFG-1 and from CEERS-93316, respectively), we carefully examine the available long-wavelength observations to investigate any possible detection of dust emission.

Because this source is not covered by our NOEMA observations, we started by looking at the deep SCUBA-2 850 μm map (Zavala et al. 2017). As shown in Figure 8 no significant detection is found (with a measured flux density of $S_{850} = -0.40 \pm 0.25$ mJy at the position of the source). We also search for significant emission in the Spitzer 8 μm and 24 μm map; Herschel 100, 160, 250, 350, and 500 μm imaging; and SCUBA-2 450 μm observations, finding only nondetections. We thus conclude that a lower-redshift scenario for Maisie's galaxy in which the source is rather associated with a DSFG is unlikely. Given the lack of far-infrared-to-submillimeter detections, the best-fit SEDs and their associated redshift probability distributions for Maisie's galaxy would be similar to those reported in Finkelstein et al. (2022a). Hence, to avoid duplication, they are not included in this Letter.

5. Conclusions

Using the available data sets from the JWST CEERS survey in combination with NOEMA and SCUBA-2 observations, we have demonstrated that DSFGs at $z \sim 4$–6 can drop out in the bluest JWST/NIRCam filters while being well detected in the redder filters. This kind of galaxies could even show a significant probability of being at high redshifts when performing SED fittings. This is illustrated by studying the source CEERS-DSFG-1, a 850 μm-selected galaxy with robust interferometric observations at 1.1 mm by NOEMA that is undetected in the F115W and F150W bands. A joint SED fitting analysis including the NIRCam constraints and the long-wavelength (sub)millimeter data implies a photometric redshift of $5.09^{+0.62}_{-0.72}$, with physical properties that resemble other DSFGs: $M_{\star} = (2.1 \pm 0.8) \times 10^{10}\,M_{\odot}$; SFR $= 110 \pm 30\,M_{\odot}\,\mathrm{yr}^{-1}$; $L_{\mathrm{dust}} = (1.1 \pm 0.3) \times 10^{12}\,L_{\odot}$. Hence, searches of $z > 10$ LBGs that rely only on a dropout selection could introduce significant contaminants from lower-redshift systems. This could be minimized by adopting multicolor selection criteria or by defining alternative conditions (such as a minimum redshift probability or χ^2 goodness-of-fit; e.g., Adams et al. 2023; Castellano et al. 2022; Donnan et al. 2023; Finkelstein et al. 2022a; Harikane et al. 2022).

[91] The $z = 10$ threshold was chosen based on the discussion presented in Appendix A. Note that other works have also followed this strategy to better assess the feasibility of low-redshift solutions (e.g., Finkelstein et al. 2022b).

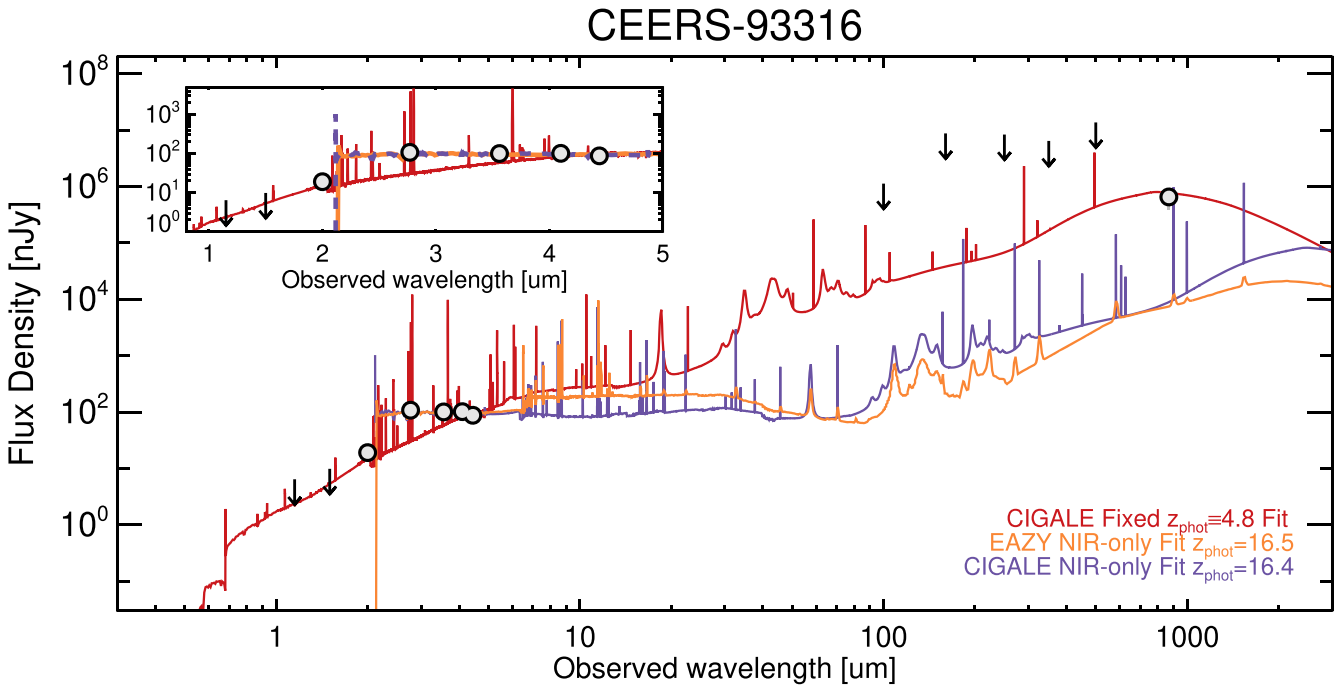

Figure 7. Best-fit spectral energy distributions for CEERS-93316. The orange and purple lines represent the $z \sim 16.4$ EAZY and CIGALE fits to the near-IR data only, which predict a 850 μm flux density significantly lower than the value implied by the tentative SCUBA-2 detection. On the other hand, the best-fit SED at $z = 4.8$ from CIGALE (red line) can reproduce both the near-IR and the submillimeter data. In this case, the blue NIRCam colors are produced by the strong emission lines, as clearly seen in the inset plot.

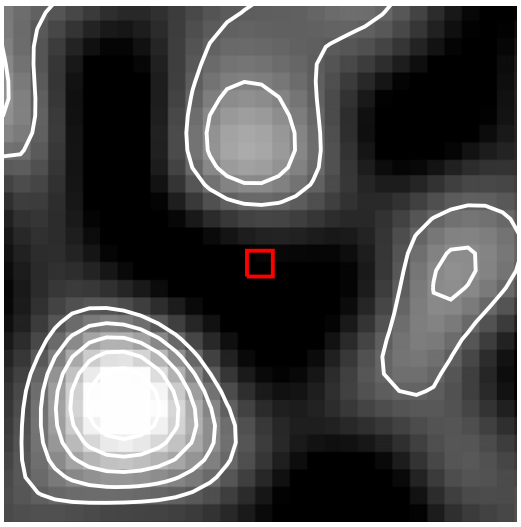

Figure 8. SCUBA-2 850 μm signal-to-noise ratio map ($60\farcs0 \times 60\farcs0$) centered at the position of Maisie's galaxy (red square; Finkelstein et al. 2022a). At the depth of the observations ($\sigma_{850\ \mu m} = 0.46$ mJy beam^{-1}), no significant dust emission is detected (the flux density at the position of the source is measured to be -0.4 ± 0.25 mJy beam^{-1}). There is also no statistical significant emission in the available Spitzer (8 and 24 μm), Herschel (100–500 μm), or SCUBA-2 (450 μm) maps.

Taking advantage of the available submillimeter data in the field, we extended the search for dust continuum emission to two close $z > 10$ LBG candidates recently reported, CEERS-93316 at $z \approx 16.7$ (Donnan et al. 2023) and Maisie's galaxy at $z \approx 11.8$ (Finkelstein et al. 2022a). We found a tentative 2.6σ detection at 850 μm around the position of CEERS-93316. A confirmation of this flux density measurement and a firm spatial association requires higher-resolution submillimeter imaging. This is particularly important given its high probability of being spurious and the large beam size ($\approx 14\farcs6$) of the SCUBA-2 observations that encompass several galaxies.

While additional observations are required to corroborate this identification, we use this possible association to illustrate that $z \sim 5$ DSFGs can also exhibit blue colors in the JWST/NIRCam bands when strong nebular emission lines are present (with line fluxes on the order of $\sim 10^{-18}$–10^{-17} erg s^{-1} cm^{-2}), and conclude that (sub)millimeter emission in samples of $z > 10$ LBGs likely implies misidentifications of DSFGs at lower redshifts ($z \lesssim 7$). Indeed, if CEERS-93316 is confirmed to be a dust emitter, our analysis suggests that it would rather lie at $z \sim 5$.

This work has illustrated both the importance and potential of combining JWST observations with submillimeter/millimeter data, a synergy that allows us to identify and characterize populations of galaxies that were previously unreachable, including both $z \gtrsim 5$ DSFGs as well as ultra-high redshift $z > 10$ LBGs. In particular, it will become crucial for searches of ultra-high redshift LBGs to closely consider contamination from lower-redshift ($z \sim 4$–7) dusty sources with significant nebular line emission that can mimic the colors of a higher-redshift Lyman break.

Despite sitting at lower redshift, new discoveries and characterizations of $z \sim 5$ DSFGs will also shed new light on an otherwise mysterious population, where fewer than a few dozen systems are currently known. Such discoveries will enable a major step forward in our understanding of massive galaxy formation in the first $\sim$1 Gyr of the universe's history.

We thank the reviewer for a constructive report that improved the clarity of our results. We also thank Jim Dunlop for helpful discussions.

V.B. and D.B. thank the Programme National de Cosmologie et Galaxies and CNES for their support. We thank Médéric

Boquien and Yannick Roehlly for their help. C.M.C. thanks the National Science Foundation for support through grants AST-1814034 and AST-2009577 and additionally the Research Corporation for Science Advancement from a 2019 Cottrell Scholar Award sponsored by IF/THEN, an initiative of Lyda Hill Philanthropies. I.A. acknowledges support from CONACyT CB-382947. We acknowledge support from STScI through award JWST-ERS-1345.

This work is based on observations made with the NASA/ESA/CSA James Webb Space Telescope. The data were obtained from the Mikulski Archive for Space Telescopes at the Space Telescope Science Institute, which is operated by the Association of Universities for Research in Astronomy, Inc., under NASA contract NAS 5-03127 for JWST. These observations are associated with program #1345 and can be accessed in a raw format via doi:10.17909/4abm-k128. This work is based on observations carried out under project number W20CK with the IRAM NOEMA Interferometer. IRAM is supported by INSU/CNRS (France), MPG (Germany) and IGN (Spain).

Facilities: JWST, NOEMA, JCMT.

Appendix A
Assessing the Reliability of High-redshift Galaxy Candidates via Dust Emission

Continuum observations at submillimeter and millimeter wavelengths probe galaxies' dust thermal emission for a wide range of redshifts. Here, adopting typical dust SEDs and relationships between dust continuum emission and other physical properties, we estimate the IR luminosity, SFR, and dust mass as a function of redshift implied by a dust continuum detection similar to the one reported in this work. Then, we compare these quantities with the expected galaxies' properties at $z > 10$ to assess whether or not they lie within the realm of high-redshift galaxies.

For these calculations, we adopt a modified blackbody distribution with a dust emissivity index of $\beta = 1.8$ for the dust SED (e.g., Casey 2012). Two different dust temperatures of 35 and 75 K are explored. Then, the IR luminosity at a given redshift is estimated by, first, scaling the redshifted SED to the 850 μm flux density and, second, integrating over 8–1000 μm (in the rest frame). The cosmic microwave background (CMB) effects on the observed flux density are also taken into account following da Cunha et al. (2013). The inferred IR luminosity as a function of redshift for a $S_{850\,\mu\mathrm{m}} = 1$ mJy dust detection is shown in the left panel of Figure 9. The corresponding dust-obscured SFR estimated directly from the IR luminosity (Kennicutt & Evans 2012) is also indicated on the right axis. Then, we calculate the dust mass as follows. At a given redshift, we estimate the rest-frame 850 μm flux density, $S_{850\,\mu\mathrm{m,rest}}$, from the scaled SED described above (which takes into account the CMB effects) and use the following equation:

$$M_{\mathrm{d}} = \frac{S_{850\,\mu\mathrm{m,rest}}\, D_L^2}{(1+z)\kappa_{\mathrm{ref}}\, B(\nu_{\mathrm{ref}}, T_{\mathrm{d}})}, \tag{A1}$$

where κ_{ref} represents the dust mass absorption coefficient at a reference wavelength and $B(\nu_{\mathrm{ref}}, T_{\mathrm{d}})$ represents the Planck function evaluated at the same frequency. We adopt $\kappa(850\,\mu\mathrm{m}) = 0.043\,\mathrm{m^2\,kg^{-1}}$ (Li & Draine 2001) for this calculation. The implied dust mass as a function of redshift is plotted in the right panel of Figure 9.

As clearly seen in Figure 9, a dust continuum detection of $S_{850\,\mu\mathrm{m}} \sim 1$ mJy (or $S_{1.1\,\mathrm{mm}} \sim 0.4$ mJy) at $z > 10$ would imply a SFR in excess of $\sim 100\,M_\odot\,\mathrm{yr^{-1}}$, rapidly reaching $\sim 1000\,M_\odot\,\mathrm{yr^{-1}}$ at $z \sim 15$ (depending on the adopted temperature). This SFR is significantly higher than what is measured in any $z \gtrsim 8$ object and around 2 orders of magnitude higher than the SFRs inferred for JWST-selected candidates. In the right panel of Figure 9, the inferred dust mass is compared with the maximum mass limit allowed by a ΛCDM universe (which depends on redshift and survey volume[92]). To estimate this limit, we use the halo mass function from the Harrison & Hotchkiss (2013) scaling; first, the halo mass down by a factor of 20 (following Marrone et al. 2018; see also Casey et al. 2021) to approximate the corresponding galaxy ISM mass, and, second, by a factor of 100, which corresponds to the ISM-to-dust ratio typically measured in massive galaxies (e.g., Magdis et al. 2012; Rémy-Ruyer et al. 2014; Scoville et al. 2016). As shown in the figure, within the volume probed by the CEERS observations, a submillimeter detection at $z \gtrsim 6$ start to be in tension (at 1σ level) with the maximum mass limit inferred from the halo mass function (when adopting $T_{\mathrm{d}} = 35$ K). This could be slightly alleviated if the dust temperature is higher. Nevertheless, Scoville et al. (2016) argue that, even when the luminosity-weighted dust temperature could be higher at higher

[92] The used survey area for the maximum halo mass calculation corresponds to 34.5 arcmin^2, the covered area by the current CEERS/NIRCam observations.

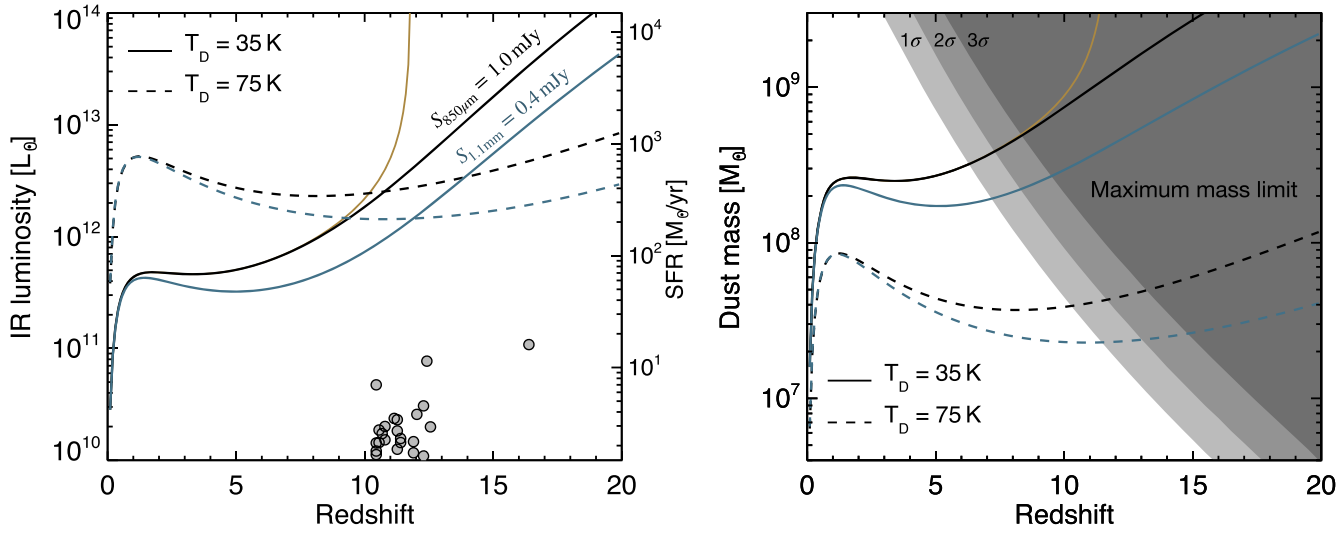

Figure 9. Left: predicted IR luminosity and SFR as a function of redshift for dust continuum detections of $S_{850\ \mu m} = 1$ mJy (black lines) and $S_{1.1\ mm} = 0.4$ mJy (blue lines), using a modified blackbody function with a dust emissivity index of $\beta = 1.8$ and dust temperature of 35 or 75 K (solid and dashed lines, respectively). For comparison, we show the SFRs of all the $z > 10$ galaxy candidates reported by Donnan et al. (2023) based on JWST/NIRCam observations in several fields. Note that the CMB effects are taken into account following da Cunha et al. (2013). The yellow line shows the predictions ignoring the extra heating produced by CMB photons, which results in a lack of contrast between the CMB and the dust emission at any redshift greater than $T_D = T_{CMB}(z)$ (for clarity, this is only shown for the 850 μm emission and for $T_D = 35$ K). Right: predicted dust mass as a function of redshift for the same set of SEDs. In addition, we plot the exclusion curves at 1σ, 2σ, and 3σ in the mass–redshift plane to illustrate the maximum dust mass of a galaxy allowed by ΛCDM cosmology within the volume covered by CEERS (see details in the main text). Based on these results, we conclude that any submillimeter/millimeter detection in the CEERS field (or any other field of similar area) with a flux density similar to that from CEERS-DSFG-1 or from the tentative emission around CEERS-93316 is unlikely to come from a $z \gtrsim 10$ galaxy.

redshifts (e.g., Faisst et al. 2017; Bakx et al. 2020; Sommovigo et al. 2022), the mass-weighted temperature is usually cold (≈25–35 K). Furthermore, even adopting the results from this relatively high dust temperature at face value, the implied dust masses exceed the expected mass limit at $z \gtrsim 12$, implying that such a system is unlikely to exist.

While these estimates represent zero-order approximations and depend strongly on the adopted assumptions (which might not be valid at very high redshifts), it is clear that dust continuum detections (on the order of $S_{850\ \mu m} \sim 1$ mJy) strongly disfavor high redshifts, $z > 10$, solutions for galaxies discovered in small surveys such as those conducted to date by the JWST. Submillimeter/millimeter surveys can thus be used to efficiently identify lower-redshift interlopers (i.e., dusty, star-forming galaxies) in samples of very high-redshift galaxy candidates.

Appendix B
Extracted Photometry for CEERS-93316

The photometry used during the SED fitting procedure on CEERS-93316 is listed in Table 3. Our fluxes are systematically brighter than those reported by Donnan et al. (2023) in all the detected bands, although the difference is small (with an average magnitude difference of −0.09 mag). This could be related to the different processes used to reduce the data and the applied correction factors as discussed in Finkelstein et al. (2022b).

Table 3
Measured Photometry of CEERS-93316

Instrument/Filter	Wavelength	Flux Density
NIRCam/F115W	1.15 μm	-4.1 ± 5.9 nJy
NIRCam/F150W	1.50 μm	7.0 ± 6.7 nJy
NIRCam/F200W	2.00 μm	22.5 ± 4.9 nJy
NIRCam/F277W	2.77 μm	94.2 ± 4.6 nJy
NIRCam/F356W	3.56 μm	95.8 ± 3.7 nJy
NIRCam/F410M	4.10 μm	102.4 ± 7.3 nJy
NIRCam/F444W	4.44 μm	89.7 ± 5.4 nJy
SCUBA-2/850 μm	850 μm	0.65 ± 0.26 mJy

ORCID iDs

Jorge A. Zavala https://orcid.org/0000-0002-7051-1100
Véronique Buat https://orcid.org/0000-0003-3441-903X
Caitlin M. Casey https://orcid.org/0000-0002-0930-6466
Steven L. Finkelstein https://orcid.org/0000-0001-8519-1130
Denis Burgarella https://orcid.org/0000-0002-4193-2539
Micaela B. Bagley https://orcid.org/0000-0002-9921-9218
Laure Ciesla https://orcid.org/0000-0003-0541-2891
Emanuele Daddi https://orcid.org/0000-0002-3331-9590
Mark Dickinson https://orcid.org/0000-0001-5414-5131
Henry C. Ferguson https://orcid.org/0000-0001-7113-2738
Maximilien Franco https://orcid.org/0000-0002-3560-8599
E. F. Jiménez-Andrade https://orcid.org/0000-0002-2640-5917
Jeyhan S. Kartaltepe https://orcid.org/0000-0001-9187-3605
Anton M. Koekemoer https://orcid.org/0000-0002-6610-2048
Aurélien Le Bail https://orcid.org/0000-0002-9466-2763
E. J. Murphy https://orcid.org/0000-0001-7089-7325
Casey Papovich https://orcid.org/0000-0001-7503-8482
Sandro Tacchella https://orcid.org/0000-0002-8224-4505
Stephen M. Wilkins https://orcid.org/0000-0003-3903-6935
Itziar Aretxaga https://orcid.org/0000-0002-6590-3994
Peter Behroozi https://orcid.org/0000-0002-2517-6446
Jaclyn B. Champagne https://orcid.org/0000-0002-6184-9097
Adriano Fontana https://orcid.org/0000-0003-3820-2823
Mauro Giavalisco https://orcid.org/0000-0002-7831-8751
Andrea Grazian https://orcid.org/0000-0002-5688-0663
Norman A. Grogin https://orcid.org/0000-0001-9440-8872
Lisa J. Kewley https://orcid.org/0000-0001-8152-3943
Dale D. Kocevski https://orcid.org/0000-0002-8360-3880
Allison Kirkpatrick https://orcid.org/0000-0002-5537-8110
Jennifer M. Lotz https://orcid.org/0000-0003-3130-5643
Laura Pentericci https://orcid.org/0000-0001-8940-6768
Pablo G. Pérez-González https://orcid.org/0000-0003-4528-5639
Nor Pirzkal https://orcid.org/0000-0003-3382-5941
Swara Ravindranath https://orcid.org/0000-0002-5269-6527
Rachel S. Somerville https://orcid.org/0000-0002-6748-6821
Jonathan R. Trump https://orcid.org/0000-0002-1410-0470
Guang Yang https://orcid.org/0000-0001-8835-7722
L. Y. Aaron Yung https://orcid.org/0000-0003-3466-035X
Omar Almaini https://orcid.org/0000-0001-9328-3991
Ricardo O. Amorín https://orcid.org/0000-0001-5758-1000
Marianna Annunziatella https://orcid.org/0000-0002-8053-8040
Pablo Arrabal Haro https://orcid.org/0000-0002-7959-8783
Bren E. Backhaus https://orcid.org/0000-0001-8534-7502
Guillermo Barro https://orcid.org/0000-0001-6813-875X
Eric F. Bell https://orcid.org/0000-0002-5564-9873
Rachana Bhatawdekar https://orcid.org/0000-0003-0883-2226
Laura Bisigello https://orcid.org/0000-0003-0492-4924
Fernando Buitrago https://orcid.org/0000-0002-2861-9812
Antonello Calabrò https://orcid.org/0000-0003-2536-1614
Marco Castellano https://orcid.org/0000-0001-9875-8263
Óscar A. Chávez Ortiz https://orcid.org/0000-0003-2332-5505
Katherine Chworowsky https://orcid.org/0000-0003-4922-0613
Nikko J. Cleri https://orcid.org/0000-0001-7151-009X
Seth H. Cohen https://orcid.org/0000-0003-3329-1337
Justin W. Cole https://orcid.org/0000-0002-6348-1900
Kevin C. Cooke https://orcid.org/0000-0002-2200-9845
M. C. Cooper https://orcid.org/0000-0003-1371-6019
Asantha R. Cooray https://orcid.org/0000-0002-3892-0190
Luca Costantin https://orcid.org/0000-0001-6820-0015
Isabella G. Cox https://orcid.org/0000-0002-1803-794X
Darren Croton https://orcid.org/0000-0002-5009-512X
Romeel Davé https://orcid.org/0000-0003-2842-9434
Alexander de la Vega https://orcid.org/0000-0002-6219-5558
Avishai Dekel https://orcid.org/0000-0003-4174-0374
David Elbaz https://orcid.org/0000-0002-7631-647X
Vicente Estrada-Carpenter https://orcid.org/0000-0001-8489-2349
Vital Fernández https://orcid.org/0000-0003-0531-5450
Keely D. Finkelstein https://orcid.org/0000-0003-0792-5877
Jonathan Freundlich https://orcid.org/0000-0002-5245-7796
Seiji Fujimoto https://orcid.org/0000-0001-7201-5066
Ángela García-Argumánez https://orcid.org/0000-0002-8365-5525
Jonathan P. Gardner https://orcid.org/0000-0003-2098-9568
Eric Gawiser https://orcid.org/0000-0003-1530-8713
Carlos Gómez-Guijarro https://orcid.org/0000-0002-4085-9165
Yuchen Guo https://orcid.org/0000-0002-4162-6523
Timothy S. Hamilton https://orcid.org/0000-0002-9753-1769
Nimish P. Hathi https://orcid.org/0000-0001-6145-5090
Benne W. Holwerda https://orcid.org/0000-0002-4884-6756
Michaela Hirschmann https://orcid.org/0000-0002-3301-3321
Marc Huertas-Company https://orcid.org/0000-0002-1416-8483
Taylor A. Hutchison https://orcid.org/0000-0001-6251-4988
Kartheik G. Iyer https://orcid.org/0000-0001-9298-3523
Anne E. Jaskot https://orcid.org/0000-0002-6790-5125
Saurabh W. Jha https://orcid.org/0000-0001-8738-6011
Shardha Jogee https://orcid.org/0000-0002-1590-0568

Stéphanie Juneau https://orcid.org/0000-0002-0000-2394
Intae Jung https://orcid.org/0000-0003-1187-4240
Susan A. Kassin https://orcid.org/0000-0002-3838-8093
Peter Kurczynski https://orcid.org/0000-0002-8816-5146
Rebecca L. Larson https://orcid.org/0000-0003-2366-8858
Gene C. K. Leung https://orcid.org/0000-0002-9393-6507
Arianna S. Long https://orcid.org/0000-0002-7530-8857
Ray A. Lucas https://orcid.org/0000-0003-1581-7825
Benjamin Magnelli https://orcid.org/0000-0002-6777-6490
Jasleen Matharu https://orcid.org/0000-0002-7547-3385
Elizabeth J. McGrath https://orcid.org/0000-0001-8688-2443
Emiliano Merlin https://orcid.org/0000-0001-6870-8900
Bahram Mobasher https://orcid.org/0000-0001-5846-4404
Alexa M. Morales https://orcid.org/0000-0003-4965-0402
Jeffrey A. Newman https://orcid.org/0000-0001-8684-2222
David C. Nicholls https://orcid.org/0000-0003-0892-5203
Viraj Pandya https://orcid.org/0000-0002-2499-9205
Marc Rafelski https://orcid.org/0000-0002-9946-4731
Kaila Ronayne https://orcid.org/0000-0001-5749-5452
Caitlin Rose https://orcid.org/0000-0002-8018-3219
Russell E. Ryan, Jr. https://orcid.org/0000-0003-0894-1588
Paola Santini https://orcid.org/0000-0002-9334-8705
Lise-Marie Seillé https://orcid.org/0000-0001-7755-4755
Ekta A. Shah https://orcid.org/0000-0001-7811-9042
Lu Shen https://orcid.org/0000-0001-9495-7759
Raymond C. Simons https://orcid.org/0000-0002-6386-7299
Gregory F. Snyder https://orcid.org/0000-0002-4226-304X
Elizabeth R. Stanway https://orcid.org/0000-0002-8770-809X
Amber N. Straughn https://orcid.org/0000-0002-4772-7878
Harry I. Teplitz https://orcid.org/0000-0002-7064-5424
Brittany N. Vanderhoof https://orcid.org/0000-0002-8163-0172
Jesús Vega-Ferrero https://orcid.org/0000-0003-2338-5567
Weichen Wang https://orcid.org/0000-0002-9593-8274
Benjamin J. Weiner https://orcid.org/0000-0001-6065-7483
Christopher N. A. Willmer https://orcid.org/0000-0001-9262-9997
Stijn Wuyts https://orcid.org/0000-0003-3735-1931

References

Adams, N. J., Conselice, C. J., Ferreira, L., et al. 2023, MNRAS, 518, 4755
Aravena, M., Boogaard, L., Gónzalez-López, J., et al. 2020, ApJ, 901, 79
Atek, H., Shuntov, M., Furtak, L. J., et al. 2023, MNRAS, 519, 1201
Bagley, M. B., Finkelstein, S. L., Koekemoer, A. M., et al. 2022, arXiv:2211.02495
Bakx, T. J. L. C., Tamura, Y., Hashimoto, T., et al. 2020, MNRAS, 493, 4294
Barger, A. J., Cowie, L. L., & Wang, W. H. 2007, ApJ, 654, 764
Barro, G., Pérez-González, P. G., Gallego, J., et al. 2011, ApJS, 193, 13
Behroozi, P., Wechsler, R. H., Hearin, A. P., & Conroy, C. 2019, MNRAS, 488, 3143
Bertin, E., & Arnouts, S. 1996, A&AS, 117, 393
Boquien, M., Burgarella, D., Roehlly, Y., et al. 2019, A&A, 622, A103
Bouwens, R., Gonzalez-Lopez, J., Aravena, M., et al. 2020, ApJ, 902, 112
Boylan-Kolchin, M. 2022, arXiv:2208.01611
Brammer, G. B., van Dokkum, P. G., & Coppi, P. 2008, ApJ, 686, 1503
Bruzual, G., & Charlot, S. 2003, MNRAS, 344, 1000
Burgarella, D., Buat, V., & Iglesias-Páramo, J. 2005, MNRAS, 360, 1413
Calzetti, D., Armus, L., Bohlin, R. C., et al. 2000, ApJ, 533, 682
Cardona-Torres, L., Aretxaga, I., Montaña, A., Zavala, J. A., & Faber, S. M. 2022, MNRAS, in press
Casey, C. M. 2012, MNRAS, 425, 3094
Casey, C. M. 2020, ApJ, 900, 68
Casey, C. M., Chen, C.-C., Cowie, L. L., et al. 2013, MNRAS, 436, 1919
Casey, C. M., Narayanan, D., & Cooray, A. 2014a, PhR, 541, 45
Casey, C. M., Scoville, N. Z., Sanders, D. B., et al. 2014b, ApJ, 796, 95
Casey, C. M., Zavala, J. A., Manning, S. M., et al. 2021, ApJ, 923, 215
Casey, C. M., Zavala, J. A., Spilker, J., et al. 2018, ApJ, 862, 77
Castellano, M., Fontana, A., Treu, T., et al. 2022, ApJL, 938, L15
Chapman, S. C., Barger, A. J., Cowie, L. L., et al. 2003, ApJ, 585, 57
da Cunha, E., Groves, B., Walter, F., et al. 2013, ApJ, 766, 13
da Cunha, E., Walter, F., Smail, I. R., et al. 2015, ApJ, 806, 110
Donnan, C. T., McLeod, D. J., Dunlop, J. S., et al. 2023, MNRAS, 518, 6011
Draine, B. T., Aniano, G., Krause, O., et al. 2014, ApJ, 780, 172
Drew, P. M., & Casey, C. M. 2022, ApJ, 930, 142
Dunlop, J. S., Cirasuolo, M., & McLure, R. J. 2007, MNRAS, 376, 1054
Dwek, E., Staguhn, J., Arendt, R. G., et al. 2014, ApJL, 788, L30
Dye, S., Eales, S. A., Aretxaga, I., et al. 2008, MNRAS, 386, 1107
Faisst, A. L., Capak, P. L., Yan, L., et al. 2017, ApJ, 847, 21
Finkelstein, S. L. 2016, PASA, 33, e037
Finkelstein, S. L., Bagley, M. B., Arrabal Haro, P., et al. 2022a, ApJL, 940, L55
Finkelstein, S. L., Bagley, M. B., Ferguson, H. C., et al. 2022b, arXiv:2211.05792
Finkelstein, S. L., Dickinson, M., Ferguson, H. C., et al. 2017, The Cosmic Evolution Early Release Science (CEERS) Survey, JWST Proposal ID 1345. Cycle 0 Early Release Science
Gómez-Guijarro, C., Elbaz, D., Xiao, M., et al. 2022, A&A, 659, A196
Harikane, Y., Ouchi, M., Oguri, M., et al. 2022, arXiv:2208.01612
Harrison, I., & Hotchkiss, S. 2013, JCAP, 2013, 022
Howell, J. H., Armus, L., Mazzarella, J. M., et al. 2010, ApJ, 715, 572
Inami, H., Algera, H., Schouws, S., et al. 2022, MNRAS, 515, 3126
Kennicutt, R. C., & Evans, N. J. 2012, ARA&A, 50, 531
Khusanova, Y., Bethermin, M., Le Fèvre, O., et al. 2021, A&A, 649, A152
Koekemoer, A. M., Faber, S. M., Ferguson, H. C., et al. 2011, ApJS, 197, 36
Laporte, N., Ellis, R. S., Boone, F., et al. 2017, ApJL, 837, L21
Larson, R. L., Hutchison, T. A., Bagley, M., et al. 2022, arXiv:2211.10035
Li, A., & Draine, B. T. 2001, ApJ, 554, 778
Lovell, C. C., Harrison, I., Harikane, Y., Tacchella, S., & Wilkins, S. M. 2023, MNRAS, 518, 511
Lutz, D., Poglitsch, A., Altieri, B., et al. 2011, A&A, 532, A90
Magdis, G. E., Daddi, E., Béthermin, M., et al. 2012, ApJ, 760, 6
Magnelli, B., Elbaz, D., Chary, R. R., et al. 2009, A&A, 496, 57
Marrone, D. P., Spilker, J. S., Hayward, C. C., et al. 2018, Natur, 553, 51
Naidu, R. P., Oesch, P. A., van Dokkum, P., et al. 2022, arXiv:2207.09434
Noll, S., Burgarella, D., Giovannoli, E., et al. 2009, A&A, 507, 1793
Oliver, S. J., Bock, J., Altieri, B., et al. 2012, MNRAS, 424, 1614
Pei, Y. C. 1992, ApJ, 395, 130
Pérez-González, P. G., Barro, G., Annunziatella, M., et al. 2022, arXiv:2211.00045
Planck Collaboration, Ade, P. A. R., Aghanim, N., et al. 2016, A&A, 594, A13
Pope, A., Scott, D., Dickinson, M., et al. 2006, MNRAS, 370, 1185
Rémy-Ruyer, A., Madden, S. C., Galliano, F., et al. 2014, A&A, 563, A31
Rigby, J., Perrin, M., McElwain, M., et al. 2022, arXiv:2207.05632
Robertson, B. E. 2022, ARA&A, 60, 121
Scoville, N., Sheth, K., Aussel, H., et al. 2016, ApJ, 820, 83
Simpson, J. M., Smail, I., Swinbank, A. M., et al. 2017, ApJ, 839, 58
Sommovigo, L., Ferrara, A., Pallottini, A., et al. 2022, MNRAS, 513, 3122
Stark, D. P. 2016, ARA&A, 54, 761
Strandet, M. L., Weiss, A., Breuck, C. D., et al. 2017, ApJL, 842, L15
Tamura, Y., Mawatari, K., Hashimoto, T., et al. 2019, ApJ, 874, 27
Wang, T., Schreiber, C., Elbaz, D., et al. 2019, Natur, 572, 211
Yan, H., Ma, Z., Ling, C., et al. 2023, ApJL, 942, L9
Zavala, J. A., Aretxaga, I., Dunlop, J. S., et al. 2018a, MNRAS, 475, 5585
Zavala, J. A., Aretxaga, I., Geach, J. E., et al. 2017, MNRAS, 464, 3369
Zavala, J. A., Montaña, A., Hughes, D. H., et al. 2018b, NatAs, 2, 56